

Skin Sea Surface Temperature schemes in coupled ocean-atmosphere modeling: the impact of chlorophyll-interactive e-folding depth.

Vincenzo de Toma², Daniele Ciani¹, Yassmin Hesham Essa^{1,3,4}, Chunxue Yang¹, Vincenzo Artale¹, Andrea Pisano¹, Davide Cavaliere¹, Rosalia Santoleri¹, and Andrea Storto¹

¹ CNR-ISMAR, Consiglio Nazionale delle Ricerche, Istituto di Scienze Marine, via Fosso del Cavaliere 100, 00133 Rome, Italy.

² CNR-ISMAR, Consiglio Nazionale delle Ricerche, Istituto di Scienze Marine, Calata Porta Di Massa - Porto Di Napoli 80, 80133 Naples, Italy.

³ GUF-IAU, Goethe University Frankfurt, Institut fuer Atmosphaere und Umwelt, Frankfurt, Germany

⁴ ARC-CLAC, Agricultural Research Center, Central Laboratory for Agricultural Climate, Giza, Egypt

Correspondence to: Vincenzo de Toma (vincenzo.detoma@cnr.it)

Abstract. In this paper, we explore different prognostic methods to account for skin sea surface temperature diurnal variations in a coupled ocean-atmosphere regional model of the Mediterranean Sea. Our aim is to characterize the sensitivity of the considered methods with respect to the underlying assumption of how the solar radiation shapes the warm layer of the ocean. All existing methods truncate solar transmission coefficient at a ~~constant~~ warm layer reference depth which is constant in space and time; instead, we develop a new scheme where this latter is estimated from a chlorophyll dataset as the e-folding depth of solar transmission, therefore allowing it to vary in space and time depending on seawater's transparency conditions. ~~This allows spatial and temporal variations of the warm layer extent to depend on seawater transparency.~~ Comparison against satellite data shows that our new scheme, compared to the one already implemented within the ocean model, improves the spatially averaged diurnal signal, especially during winter, and the seasonally averaged one in spring, and autumn, while showing with a monthly, basin-wide averaged bias on monthly scales year-round smaller than 0.1 K year-round. In April, when most of the drifters' measurements are available, the new scheme mitigates the bias during nighttime, keeping it positive but smaller than 0.12 K during the rest of the monthly-averaged day. The new scheme implemented within the ocean model improves the old one by about 0.1 K, particularly during June. All the methods considered here showed differences with respect to objectively analyzed profiles confined between 0.5 K during winter and 1 K in summer for both the eastern and the western Mediterranean regions, especially over the uppermost 60 m. More in detail, the new scheme reduces the RMSE on the top 15 m in the central Mediterranean for summertime months, compared to the one already implemented one within the ocean model. Overall, the surface net total heat flux shows that the use of a skin SST parametrization brings the budget about 1.5 W/m² closer to zero on an annual basis, despite all simulations showing an annual net heat loss from the ocean to the atmosphere. Our "chlorophyll-interactive" method proved to be an effective enhancement of existing methods, its strength relying on an improved physical consistency with the solar extinction implemented in the ocean component.

ha formattato: Tipo di carattere: Corsivo

39 1 Introduction

40 Air-sea fluxes govern the energy exchange at the ocean-atmosphere interface. A reliable representation of
41 the Sea Surface Temperature (SST) diurnal cycle, i.e. the typical SST oscillation/excursion between night and
42 day mainly due to solar heating, is crucial to accurately estimate air-sea heat fluxes (Kawai and Wada, 2007,
43 Soloviev and Lukas, 2013), whose direct measurement is very difficult. Indeed, diurnal warming events can
44 often exceed 5 K depending on weather conditions (Soloviev and Lukas, 1997) and geographical location,
45 typically at tropical and mid-latitudes but also occasionally at high latitudes (Karagali and Høyer, 2013). Large
46 diurnal warming events can lead to changes in air-sea heat flux locally reaching up to $60W/m^2$ (Fairall et al.,
47 1996, Ward, 2006, Kawai and Wada, 2007, Marullo et al., 2010, Marullo et al., 2016) on a variety of scales,
48 ranging from the short regional ocean weather ones to large seasonal or long-term ones.

49
50 Therefore, there is a wide interest in the development of models to accurately reconstruct SST diurnal variations
51 in order to improve the representation of air-sea energy exchanges, especially, but not solely, within the coupled
52 ocean-atmosphere modeling framework (Penny et al., 2019).

53 The net energy flux across the air-sea interface results from four contributions: the net solar radiation; latent
54 and sensible heat fluxes, and the net thermal radiation. The last three contributions depend on SST and have a
55 direct impact in determining ocean heat uptake or dynamical processes such as deep-water formation (Chen
56 and Houze Jr., 1997). Ideally, the most accurate flux estimate would imply the knowledge of the temperature
57 right at the atmosphere-ocean separation interface. From an observational point of view, the skin SST is the
58 temperature immediately adjacent to the ocean surface (~10-20 microns depth) that is measurable, typically
59 from infrared radiometers, and thus a key parameter to understand heat flux exchange (Minnet et al., 2019).
60 Indeed, following what is measurable by current sensors, the GHRSSST-PP (i.e. the Global ocean data
61 assimilation experiment High Resolution SST Pilot Project) introduced the distinction between skin, sub-skin,
62 depth, and foundation SST (Donlon et al., 2007), which can be respectively regarded as successive, better-to-
63 worse approximations to the ideal target, i.e. SST right at the interface, which is actually impossible to measure.
64 However, in most of the widely used ocean models and configurations, the too-coarse vertical resolution does
65 not allow to direct modeling skin SST (the first model layer being only around 0.5 - 1 meter thick, e. g. the
66 ocean model NEMO – see the sketch in figure 1). Therefore, one must use schemes to reconstruct skin SST
67 variations. Sadly, the only thing one can be sure about is that in general no model will be able to perfectly
68 reproduce skin SST diurnal variations, and there are different ways to approach this challenging problem, each
69 one still with its own limitations (see Kawai and Wada, 2007 and references therein). Simplified ~~models~~
70 ~~approaches~~ widely employed in ocean and atmosphere state-of-the-art models parameterize the skin SST
71 dynamics via the distinction of two main effects: the cool skin and the warm layer. Due to its interactions with
72 the atmosphere, the temperature right at the ~~interface of separation ocean surface~~ is supposed to be almost
73 anywhere and anytime ~~cooler-lower~~ than ~~the the ones below~~ temperature of the waters infinitesimally close to
74 ~~it~~, resulting in the ocean being covered with a ~~thin~~ cool skin layer. ~~One~~ of the very first and simpler models

75 assumes this cool skin temperature difference as proportional to the ratio between heat fluxes and kinematic
76 stress (Saunders, 1967), via the Saunders' constant.

77 The cool skin effect is very important in obtaining accurate estimates of the latent and sensible heat flux,
78 especially because its consideration modifies specific humidity at the ocean surface, which is one of the factors
79 in the bulk formula. Indeed, latent and sensible heat fluxes are defined as the heat transfer across the
80 ocean/atmosphere interface due to turbulent air motions (the former including the one resulting from
81 condensation or evaporation). For example, a recent study in the South China Sea showed that during nighttime
82 the cool skin temperature difference is around 1 K, and there's currently a large uncertainty in the Saunders'
83 constant (Zhang et al., 2021⁹). A warm layer (in which diurnal warming effectively takes place) develops below
84 this cool skin, and its extent reaches a depth at which the penetration of solar radiation can be neglected (usually
85 fixed to 3m by most ~~of~~ existing parameterizations – see section 3.3 for more details). Diurnal warm layer
86 anomalies (which can sometimes exceed 3K) can potentially impact both the atmosphere and ocean mean state
87 on a variety of spatial (ranging from regional, basin-wide to global ones) and temporal scales (relevant for
88 weather or seasonal forecast to long-term climatic trends) (Donlon et al., 2007). The skin SST diurnal warming
89 amplitude increases under low surface winds (smaller than 2 m/s) and intense solar radiation (higher than
90 typical daily peaks, around 900 W/m²) conditions, smaller in winter and at the poles than in summer and in
91 the tropics. The accuracy of skin SST models, and therefore their ability to reconstruct skin SST diurnal
92 variations is crucial especially in heat budget closure problems, which are still a subject of active debate
93 especially in climate change hot spot regions such as the Mediterranean domain (see Marullo et al., 2021 and
94 references therein). Skin SST schemes are also crucial for assimilating daytime SST data from satellite sensors
95 (Penny et al., 2019; Storto and Oddo, 2019, Jansen et al., 2019), with obvious impact on the accuracy of
96 numerical weather and ocean predictions; a correct account of skin SST diurnal variations in turn is crucial for
97 flux calculations, which is already a very delicate problem also from an instrumental point of view.

98 Within these prognostic schemes, seawater's transparency conditions (e.g., estimated using chlorophyll
99 concentration) have great implications in the way solar radiation is absorbed within the ocean's uppermost layer
100 (Morel and Antoine 1994). Ohlmann et al. 2000 quantified with the help of radiative transfer calculations effects
101 of physical and biological processes on solar radiation transmission, classifying as main factors chlorophyll
102 concentration, cloud cover and solar zenith angle. Ohlmann and Siegel 2000 and Lee et al. 2005 are further
103 examples of how radiative transfer models are used to develop solar transmission parameterization which is fit
104 to the sum of exponentials (the number of terms in the sum depending on the variable which has been
105 considered). To the best of our knowledge, these ideas have not been implemented nor tested within the
106 prognostic scheme for skin SST present in the ocean model NEMO, which just relies on chlorophyll-calibrated
107 coefficients though (Gentemann et al 2009).

108 Our main aim here is therefore to improve existing skin SST prognostic schemes, investigating the impact of
109 variable ~~accounting for~~ seawater's transparency conditions in modeling solar radiation extinction in the upper
110 ocean. The use of chlorophyll concentration as a proxy for seawater's transparency is not new. In fact, given

111 its covariance with Secchi disk depth (estimated from reflectance at various wavelength), it has been often
112 applied by the ocean color community to study the dynamics of oligotrophic gyres (Leonelli et al., 2022 and
113 references therein). The paper is structured as follows: after this introduction, we describe the data and coupled
114 modeling system in section 2. The mathematical context in which we developed our new method, whose novelty
115 stands in allowing the warm layer's extent to vary in space and time according to a chlorophyll-concentration
116 climatology follows in section 3. In section 4 we present results, discussing them and drawing conclusions in
117 section 5.

118 **2 Data and Modeling System**

119 We describe here the data and the coupled regional modeling system used in this study. Our description
120 here is functional to the scope of this paper, and far from a complete depiction of each dataset. We refer readers
121 to the documentation and relevant literature for detailed information on each dataset and model.

122 **2**
123 Operational MED DOISST within CMEMS
124 We describe here the data and the coupled regional modeling
125 system used in this study. Our description here is functional to the scope of this paper, and far from a complete
126 depiction of each dataset. We redirect the documentation and the appropriate literature describing each data and
127 model in depth.

127 **2.1 Operational MED DOISST within CMEMS**

128 The MEDiterranean Diurnal Optimally Interpolated Sea Surface Temperature (MED DOISST) product,
129 operationally distributed and freely available within the Copernicus Marine Environmental Service (CMEMS)
130 provides gap-free (L4) hourly mean maps of sub-skin SST at 1/16° horizontal resolution over the Mediterranean
131 domain, covering from 2019 to present. Sub-skin SST is defined as the temperature at the base of the cool skin
132 layer, typically sensed by microwave radiometers, and representative of a depth of few millimeters from the
133 ocean's surface (Minnet et al., 2019).

134
135 This product combines satellite data acquired from the Spinning Enhanced Visible and InfraRed Imager
136 (SEVIRI) and model data from the Mediterranean Forecasting System (MedFS), respectively used as
137 observations and first guess for an optimal interpolation, giving a L4 field representative of subskin SST (see
138 Pisano et al., 2022 and references therein). In all diagnostics involving these data (and presented in the following
139 sections), regions where the percentage of model data valid SEVIRI measurements is higher-lower than 50%
140 have been masked out both in CMEMS MED DOISST and our experiments.

141 **2.1.2 iQuam in-situ data**

142 SST from drifter data were used for validation purposes and acquired from the iQuam (In situ SST Quality
143 Monitor) archive (Xu and Ignatov, 2014). The iQuam provides high-quality and quality controlled (QC) in-situ
144 SST data collected from various platforms, such as drifters, Argo Floats, ships, tropical and coastal moored

Formattato: Rientro: Prima riga: 0,81 cm, Interlinea: 1,5 righe

ha formattato: Tipo di carattere: (Predefinito) Cambria, 11 pt

Formattato: Normale, Allineato a sinistra, Destro 0 cm, Interlinea: singola, Nessun elenco puntato o numerato

Formattato: Titolo 2, Destro 0 cm, SpazioDopo: 0 pt, Interlinea: singola, Struttura + Livello:2 + Stile numerazione: 1, 2, 3, ... + Comincia da:1 + Allineamento: A sinistra + Allinea a: 0 cm + Imposta un rientro di: 0 cm

145 buoys. iQuam SST data are also provided along with quality level flags ranging from 0 to 5, with 5
146 corresponding to the highest quality level (Xu and Ignatov, 2014). For this study, SST with quality level equal
147 five were selected from drifters only, since they provide the temperature measurement closest to the surface
148 (compared to the other available instruments), ranging between 20-30cm (depending on the drifter type).

149
150 Additionally, we interpolated model outputs on drifters' location in time and space. Table S1 [resumes-outlines](#)
151 the number of available measurements for each given month and hour of the day. A total number of 555919
152 records were available after the quality flag and platform selection, with the month of April being the most
153 populated one, with 222996 measurements, and 10361 measurements at 9:00 am.

154 [2-2.2.3 EN4 objective analysis](#)

156 EN4, the quality controlled subsurface ocean temperature and salinity profiles and objective analyses, were
157 used to assess the impact on the temperature vertical profiles. To facilitate the comparison, we made use of the
158 objective analyses after bias corrections of Expendable Bathythermograph (XBT) calibrations (Gouretski and
159 Reseghetti, 2010, Gouretski and Cheng, 2020), which give a gridded version of the dataset on a 1-degree regular
160 grid. In the comparison, model outputs were interpolated on this grid.

161 [2-3.2.4 Mediterranean Chlorophyll concentration](#)

162 Chlorophyll data were used to estimate e-folding depths' seasonality (see Methods, Section 3). These data
163 are a daily interpolation at 0.3 km horizontal resolution over the Mediterranean domain, and result from a
164 merging between multiple sensors (MERIS - MEdium Resolution Imaging Spectrometer from ESA, SeaWiFS
165 - Sea-viewing Wide Field-of-view Sensor and MODIS - Moderate Resolution Imaging Spectroradiometer from
166 NASA, VIIRS - Visible Infrared Imager Radiometer Suite from NOAA, and most recently the Copernicus
167 Sentinel 3A OLCI - Ocean and Land Colour Instrument), as detailed in the product description (see Volpe et
168 al., 2019 and references therein for further details).

169 [2-4.2.5 ECMWF Atmospheric Reanalysis - ERA5](#)

171 We used heat fluxes (net solar radiation, latent and sensible heat fluxes, net thermal radiation) from ERA5
172 at 0.25° horizontal and hourly temporal resolution (Hersbach et al., 2020) as reference for comparing
173 performances across simulations with different skin SST schemes. Despite their possible biases in air-sea fluxes,
174 atmospheric reanalyses [at-daytoday](#) are still widely thought to provide the best gap-free and dynamically
175 consistent reconstructions of the atmosphere system (Valdivieso et al., 2017, Storto et al., 2019).

176 [2-5.2.6 Mixed Layer Depth 1969-2013 Climatology](#)

178 Data from a mixed layer depth (MLD) climatology was used to test to what extent our modified scheme
179 correctly represents the seasonality of the mixed layer.
180 This monthly gridded climatology was produced using MBT, XBT, Profiling floats, Gliders, and ship-based
181 CTD (Conductivity, Temperature, Depth) data from different databases and carried out in the Mediterranean
182 Sea between 1969 and 2013. As for the model outputs, MLD is calculated with a $\Delta T = 0.1^\circ\text{C}$ criterion relative
183 to 10m reference level on individual profiles (Houpert et al., 2015a, Houpert et al., 2015b).

185 [2.6.2.7](#) ISMAR Mediterranean Earth System Model (MESMAR)

186 MESMAR is a newly developed coupled regional modeling framework for the Mediterranean region (Storto
187 et al., 2023). MESMAR includes the following components:

- 188 • the ocean model: NEMO v4.0.7, with horizontal resolution of about 7 km, 72 [unevenly spaced](#) vertical
189 levels [\(the first and the last levels being respectively about 0.5m and 200m thick\)](#) and a timestep of 7.5
190 minutes (NEMO System Team, 2019);
- 191 • the atmosphere model: WRF v4.3.3, with 41 vertical hybrid levels and horizontal resolution of about 15
192 km, covering the European branch of the international Coordinated Downscaling Experiment (EURO-
193 CORDEX) domain, and a timestep of 1 minute (Skamarock et al., 2019);
- 194 • an interactive runoff model: HD v5.0.1, with a timestep of 30 minutes and $1/12^\circ$ degree horizontal
195 resolution over Europe (Hagemann et al., 2020);
- 196 • the coupler: OASIS3-MCT, coupling the three models with a coupling frequency of 30 minutes, and
197 using the SCRIP library to interpolate fields between different model grids (Craig et al., 2017) ;

198 We report in figure [24](#) a graphical summary of different grids. Further details of its implementation, tuning,
199 and performances are described in (Storto et al., 2023).

200

201 3 Methods

202 Many schemes to reconstruct the skin SST diurnal variations rely on the existence of a cool skin and a warm
203 layer, respectively in the upper micrometers and few meters of the ocean, whose dynamics strongly depends on
204 wind conditions and solar radiation extinction within the upper ocean. To explain the rationale behind the
205 developments in our new method, we need to recap here some elements of this theory, which is mostly based
206 on Zeng and Beljaars, 2005 (named ZB05 hereafter) work.

207 We start from the one-dimensional heat transfer equation in the ocean:

$$208 \quad \frac{\partial T}{\partial t} = \frac{\partial}{\partial z} (K_w + k_w) \frac{\partial T}{\partial z} + \frac{1}{\rho_w c_w} \frac{\partial R}{\partial z} \quad (1)$$

in which the subscript w refers to water properties, T is seawater temperature (K), K_w ($m^2 s^{-1}$) is the turbulent diffusion coefficient, k_w ($m^2 s^{-1}$) is the molecular thermal conductivity, ρ_w ($Kg m^{-3}$), c_w ($J Kg^{-1} K^{-1}$) are respectively seawater density and heat capacity per unit volume, R ($W m^{-2}$) is the net solar radiation flux, defined as positive downward.

ha formattato: Tipo di carattere: Non Corsivo

ha formattato: Tipo di carattere: Non Corsivo

3.1 Cool Skin

We assume that there exists an oceanic molecular sublayer of depth δ , where K_w is negligible, and temperature can be assumed constant in time, since it is always cooler than temperature of the underlying seawater (Donlon et al., 2007, Zeng and Beljaars, 2005). Then integration of eqn. (1) gives, $\forall z \in [0, -\delta]$

$$k_w \frac{\partial T}{\partial z} + \frac{1}{\rho_w c_w} [R(z) - R_s] - k_w \frac{\partial^2 T}{\partial z^2} = const, \quad \mathcal{O}(z^2) \quad (2)$$

where R_s is the net solar radiation at the surface (constant, open-ocean albedo, since the Mediterranean Sea is an ice-free basin), assuming this constant to be the top boundary condition at $z = 0$:

$$\rho_w c_w k_w \left. \frac{\partial T}{\partial z} \right|_{z=0} = Q = LH + SH + LW, \quad (3)$$

in which LH , SH , LW are respectively the surface fluxes of latent, sensible heat and net long wave radiation.

Thus, eqn. (2) can be rewritten as

$$\rho_w c_w k_w \frac{\partial T}{\partial z} = Q + R_s - R(z). \quad (4)$$

Making a further integration we get the cool skin temperature difference:

$$T_s - T_{-\delta} = \frac{\delta}{\rho_w c_w k_w} (Q + f_s R_s), \quad (5)$$

where T_s and $T_{-\delta}$ are respectively the temperature at the upper (air-sea interface) and lower limits of the cool skin layer, while f_s is the fraction of solar radiation absorbed in this layer:

$$f_s = \frac{1}{\delta} \int_{-\delta}^0 \left(1 - \frac{R(z)}{R_s} \right) dz,$$

which depends on the way radiation gets absorbed within the cool skin. Being time-independent, the cool skin temperature difference is a diagnostic variable in the scheme.

Eq. (5) is analogous to Saunders' model. Indeed, Saunders, 1967 was one of the first to construct a theory for the ocean "cool skin" effect (already known from decades at those times), i.e. the observed temperature at the air-sea interface is generally cooler than the temperature of the water at about 10 cm depth, especially during nighttime. This effect takes place mainly because of the transfer of energy between the ocean and the

237 atmosphere, realized via heat loss and momentum transfers (wind stress). In a nutshell, at the end of its
 238 derivation (Saunders, 1967), he obtains the following expression for the temperature difference across the cool
 239 skin, ΔT_c (K):

$$\Delta T_c = \lambda \frac{Q v_w}{k_w (\tau / \rho_w)^{1/2}}, \quad (6)$$

241 where λ is the Saunders' proportionality constant, Q ($W m^{-2}$) has already been defined above, τ / ρ_w ($m^2 s^{-2}$) is the
 242 kinematic stress (ratio between wind stress module and seawater density), and v_w ($m^2 s^{-1}$) k_w ($m^2 s^{-1}$) are
 243 respectively the kinematic viscosity and thermal conductivity of seawater. Saunders' formulation was originally
 244 conceived for low, nonzero wind conditions and neglecting the effect of solar radiation (which however
 245 recognized its role and added a discussion on how to account for it in the model only at the end of his paper).
 246 As noticed by Fairall et al. 1996, Artale et al., 2002 (named A02 hereafter), with a constant λ , eqn. (6) becomes
 247 problematic in limiting cases of low and very high wind speeds (greater than 7 m/s), because the wind stress
 248 in the denominator limits its validity. Thus, they-A02 proposed to include a wind dependence in Saunders'
 249 constant, in order to still have a finite, nonzero cool skin to bulk temperature difference even when the wind
 250 speed goes to zero or becomes very high.

251 This scheme has proven to have good performances compared to other schemes also on a mooring site in the
 252 Pacific Ocean (Tu and Tsuang, 2005).

254 3.2 Warm Layer

255 Below the skin layer, turbulent transfer is much more effective, and k_w can be neglected in favor of K_w .
 256 Integrating eqn. (1) within the $[-d, -\delta]$ layer, we get:

$$\frac{\partial}{\partial t} \int_{-d}^{-\delta} T dz = \frac{Q + R_s - R(-d)}{\rho_w c_w} - K_w \left. \frac{\partial T}{\partial z} \right|_{z=-d}, \quad (7)$$

258 where d is a reference depth which can be assumed as the depth at which the diurnal
 259 cycle can be omitted.

260 The turbulent diffusion coefficient can be expressed as (Large et al., 1994):

$$K_w = k u_{*w} (-z) / \phi_t \left(\frac{-z}{L} \right), \quad (8)$$

262 in which $k = 0.4$ is the Von Karman constant, z is negative in the ocean, u_{*w} is the friction velocity in the water
 263 (this being the air friction velocity multiplied by the square root of air to sea density ratio), and the stability
 264 function ϕ_t discriminates between a stable and an unstable regime, depending on the sign of its argument, which
 265 is the ratio of the vertical coordinate to the Monin Obukhov length L : positive for the stable and negative for
 266 the unstable one. Assuming z to be negative in the ocean, the change of sign entirely depends on the Monin
 267 Obukhov length, which is a length characterizing the prevalence of buoyancy variations induced turbulence

Formattato: Rientro: Sinistro: 0 cm

ha formattato: Tipo di carattere: Corsivo

over the one generated by wind shear effects. This in turn is strongly dependent on the sign of the net heat flux Q . If $Q > 0$, i.e. the ocean gains heat from the atmosphere, and we have the stable regime: the diffusion coefficients decrease with increasing depth, favoring the downward heat transfer within the water column. The opposite case, which favors transfer of heat from the ocean to the atmosphere, can be modeled in different ways (see While et al., 2017 and references therein).

Assuming a temperature-~~of~~ dependence, for $d \gg \delta$ of the form

$$T = T_{-\delta} - \left[\frac{z + \delta}{-d + \delta} \right]^\nu (T_{-\delta} - T_{-d}), \quad \nu \text{ empirical parameter} \quad (9)$$

eqn. (7) simplifies to

$$\frac{\partial}{\partial t} (T_{-\delta} - T_{-d}) = \frac{Q + R_s - R(-d)}{d\rho_w c_w} \frac{\nu + 1}{\nu} - \frac{(\nu + 1)ku_{*w}}{d\phi_t(d/L)} (T_{-\delta} - T_{-d}) \quad (10)$$

In ZB05 scheme (Zeng and Beljaars, 2005), eqs. (5, 10) are the coupled equations for the cool skin (diagnostic part) and warm layer (prognostic part) respectively. Being time dependent, the determination of the warm layer temperature difference at time t requires the knowledge of the one at the previous time step, and thus is the prognostic variable in the scheme. Assumptions on the fraction of solar radiation within ~~this layer~~ the warm layer and the cool skin depth usually follow Fairall et al., 1996 parameterization, whose detail are given in the Supplementary Material section.

3.3 Solar transmission expression

The expression of the solar transmission in Zeng and Beljaars, 2005 is

$$\frac{R(-d)}{R_s} = \sum_{i=1}^3 a_i e^{-db_i}, \quad (a_1, a_2, a_3) = (0.28, 0.27, 0.45), \\ (b_1, b_2, b_3) = (71.5, 2.8, 0.07)m^{-1},$$

following Soloviev formulation (Soloviev, 1982) (S82 in the following), which is very widely used in atmosphere models (such as WRF, Skamarock et al., 2019).

So far this is not the only possibility: a formulation with 61 coefficients has been developed by Jerlov, 1968, which is based on different water types classified based on chlorophyll concentration and particulates, for light in the visible spectrum.

~~A formulation~~ Formulations with 9 coefficients (reported in Table 2) ~~has-have~~ been proposed to include such effects: for example ~~←~~ Soloviev and Schlüssel, 1996 use a different coefficient for the first term depending on Jerlov's optical water type, while Gentemann et al., 2009 include solar angle in the parameterization, keeping the value of the of the first coefficient as in the case of pure-water, Gentemann et al., 2009). Without knowing what the Jerlov water type is, what is currently implemented in NEMO is to take b_1 as ~~the first of them~~

299 ~~accounting for mean properties- the average between coefficients for~~ I, IA, IB, II and III Jerlov's optical water
300 types. This formulation is widely employed in ocean models (such as in the optional skin SST routine of NEMO,
301 see While et al., 2017), with the reference depth d fixed to 3 m. So, the solar transmission ~~coefficient~~ follows
302 as:

$$\frac{R(-d)}{R_s} = \sum_{i=1}^9 a_i e^{-db_i} \quad (13)$$

303
304 Ideally, one would like to have a reference depth representative of the one at which the transmission of solar
305 radiation is negligible, and if we take it as the depth at which transmission drops ~~by-to~~ $1/e$ from its surface value,
306 we get a value which can be different from $d = 3$ m, as we can see from figure 32a. Allowing for a realistic time
307 and space varying value of d represents the main novelty of our work.

308
309 From this viewpoint, choosing a value of $d = 3$ m while using the solar extinction formulation as in Soloviev,
310 1982 or Soloviev and Schlüssel, 1996 would lead to underestimatinge the penetration of solar radiation into the
311 warm layer. Another possibility, which constitutes our modification to the scheme already implemented in
312 NEMO as in the case of the NEMO module for radiation calculations (Jerlov, 1968, Morel et al., 1989,
313 Lengaigne et al., 2007), is to reconstruct a chlorophyll profile from its surface values following what is already
314 implemented in the as in the case of the NEMO module for radiation calculations (Jerlov, 1968, Morel et al.,
315 1989, Lengaigne et al., 2007), and employ an R-G-B+Chl-a scheme to calculate radiation as a function of depth.
316 Then, From from eqn. (13) with only 4 terms (one for chlorophyll, and three for R-G-B, expressed in lookup
317 tables), one can numerically derive the warm layer reference depth as the e-folding depth of the light extinction
318 profile (see Fortran source files in the Zenodo repository, de Toma (2024)) using chlorophyll variations and the
319 R-G-B light extinction coefficients taken from lookup tables in the source code.

320
321 This would give a constant transmission throughout the basin, but with a spatially and temporally varying e-
322 folding depth and defines our new prognostic scheme for skin SST warm layer calculation, thus embedding in
323 it the ocean color information coming from Chl-a. Everything else is left unchanged, both the refinements of
324 Takaya et al., 2010, which include the effect of Langmuir circulation and a modification of the Monin-Obukhov
325 similarity function under stable conditions (T10 hereafter), and the A02 model for cool skin, which has been
326 demonstrated to improve the scheme respectively under wavy and windy conditions.

327 3.3.1 E-folding depth estimates

328 Mediterranean Chlorophyll climatology data (see section 2.4) were re-gridded onto a 0.25° regular
329 longitude/latitude grid, and tabulated coefficients within NEMO were used to retrieve the transmission,
330 accounting for chlorophyll variations. E-folding depths then can be estimated as the depth at which transmission
331 drops ~~by-to~~ $1/e$ from its surface value. It can be noticed from figure 32b that also the e-folding depth varies with
332 seasonality, with typical values ranging from about 3 to 4.5 meters. This is the central point of our modification

333 to the prognostic scheme. In our setup we extracted pixelwise and at each time step of the NEMO model the e-
334 folding depth used within the prognostic scheme.

335 3.4 Overview of the simulations performed.

336 With the coupled ocean-atmosphere regional system we performed a set of four simulations, forced by
337 ERA5 in the atmosphere and ORAS5 (Zuo et al., 2018) in the ocean and covering three years (from 2019 to
338 2021), with hourly outputs (a synthesis is provided in Table 1). In cases where a skin SST scheme is active, we
339 substitute the SST, i.e. temperature on the first NEMO level, with the skin SST coming out from the scheme:

- 340 1. a control run, in which no skin SST prognostic scheme is activated, therefore the diurnal SST variations
341 in the uppermost ocean layer (0.5 m thick) only come from the variability represented by the ocean model
342 at about 0.5 m of depth, considering also the 0.5 hours frequency of the coupling. We will refer to this
343 experiment in the following as *ctrlnoskin*;
- 344 2. a run in which the ZB05 scheme in WRF (Zeng and Beljaars, 2005) is active -- we shall refer to this case
345 in the following as *wrfskin*;
- 346 3. a run in which the existing scheme within NEMO, which employ the 9-coefficient parameterization for
347 light extinction coefficients (Gentemann et al., 2009 -- G09 hereafter), the scheme for the cool skin as
348 modified in A02, and refinements of the stability function, in the warm layer formulation as in T10 -- we
349 shall refer to this as the *nemoskwrite* case;
- 350 4. a fourth simulation in which we modified the reference depth for the basis of the warm layer from $z = 3$
351 m , to an e-folding depth (i.e. the depth at which radiation gets diminished by $1/e$ from its surface value),
352 which is allowed to vary temporally and spatially because it is estimated from R-G-B light extinction
353 coefficients and chlorophyll concentration (see section 3) ~~below~~. We will refer to it as *modradnemo*,
354 being the experiment where our modification to the skin SST scheme is implemented and tested.

355 The reason behind the choice of the above mentioned period of three years 2019-2021 is twofold: firstly, it
356 allows a validation against all the measurements from different data sources (satellite, drifters and objectively
357 analyzed profiles), and secondly, it is a good trade-off between the needs of keeping a reasonable computational
358 load, data volume for the analysis, and guarantees a minimal robustness of our finding, compared to a simulation
359 which covers just one year. However, we do not discard the possibility to extend the time coverage in our plans
360 for future works.

361 4 Results

362 In this section, we present skill scores against satellite, drifters and temperature profiles data (see section 2)
363 from the set of the simulations performed, aimed at characterizing the impacts of our modified skin SST scheme.
364 ~~we compare simulations outputs with data from different sources (see section 2), to assess methods~~

performances and impacts of our modifications. Since we are mainly acting to improve skin SST diurnal variations reconstruction in the ocean component, the main focus is on the difference between the nemoskwrite and modradnemo, while the ctrlnoskin and wrfskin ones are included as further reference elements (the latter being not directly comparable because the atmospheric model sees the ocean foundation SST and employ the scheme just to diagnose the skinSST).

4.1 Comparison with CMEMS MED DOISST

We calculated the mean diurnal warming amplitude in each season as the seasonally averaged diurnal warming amplitudes (diurnal warming amplitude being defined for each day as the difference between daytime maximum and nighttime minimum of SST), which can be cast into the following equation:

$$\langle \text{DWA} \rangle_{\text{seas}} = \frac{1}{N_{\text{seas}}} \sum_{i=1}^{N_{\text{seas}}} \left\{ \max_{h_i \in [10:00, 18:00]} \text{SST}(h_i) - \min_{h_i \in [00:00, 06:00]} \text{SST}(h_i) \right\},$$

$$\langle \text{DWA} \rangle_{\text{seas}} = \frac{1}{N_{\text{seas}}} \sum_{i=0}^{N_{\text{seas}}} \left\{ \max_{h_i \in [10:00, 18:00]} - \min_{h_i \in [00:00, 06:00]} \right\} \text{SST}(h_i), \quad (14)$$

where seas = DJF, JJA, MAM, SON is the given season, N_{seas} is the number of days in that particular season and h_i is the local time in hours for any given day.

Seasonally averaged diurnal warming amplitudes are shown in figure 43. On average, the maximum amplitude is reached in summer, with the wrfskin simulation peaking at about 3 K, thus overestimating the mean diurnal cycle compared to CMEMS MED DOISST (the monthly biases with respect to CMEMS foundation SST both in the western and the eastern part of the Mediterranean Sea stay below 1 K year-round for every-all of the simulations performed – see figure S1 in Supplementary Materials). The nemoskwrite simulation yields a pattern very similar to CMEMS MED DOISST in summer, but underestimates the signal in the remaining seasons. Outside the Summer season, our modifications yield a slight improvement (see modradnemo, last row of figure 43). As expected, the control run in which no skin SST method is active, generally underestimates the diurnal signal everywhere. Compared to nemoskwrite, the modradnemo simulation improves JJA mean diurnal warming amplitude, especially over the Southern Mediterranean Sea, while in central and Northern part of the basin tends to overestimate the signal by about 0.5 K with respect to CMEMS-DOI data. Furthermore, a general underestimation is present also in DJF, with the modradnemo simulation showing the smallest differences with respect to CMEMS-DOI data.

The spatial average over the whole Mediterranean domain is shown in figure 54, confirming the general underestimation of the control run and the overestimation of the wrfskin (ZB05 scheme) and modradnemo in all seasons except winter.

395 ~~Computing spatial averages~~ Spatially averaging highlights that modradnemo slightly improves the mean diurnal
396 ~~warming amplitude signal during wintertime, our modification brings improvement, especially during~~
397 ~~wintertime~~, while in all the other seasons the best agreement is gained by using the nemoskwrite setup (ZB05
398 with T10 and A02 modifications), at least according to the verification against CMEMS MED DOISST.

399 On a monthly timescale, figure 65 confirms that the control simulation tends generally to have a negative bias
400 of the diurnal amplitude, for the whole simulated period. The wrfskin (ZB05 scheme) shows a warm bias during
401 summertime months, shown just as a reference. The comparison between nemoskwrite (ZB05+A02+T10) and
402 modradnemo (chl e-folding depth) shows improvement of our scheme (modradnemo) over the old one
403 (nemoskwrite) especially in May, but not in ~~April, June, July, August and September~~, despite in the rest of the
404 period the amplitude of the bias is slightly reduced.

405 4.2 Comparison with iQuam Star HR-Drifters

406 The bias with respect to drifter measurements averaged over drifters positions as a function of the month
407 and time of the day is shown in figure 76. All the schemes present a systematic cool bias in autumn (SON) for
408 most of the hours of the day. During April and June, the modradnemo simulation significantly reduced the
409 warm bias with respect to observations, compared to the nemoskwrite case, keeping it however generally
410 positive. This is quite reasonable, since drifters measurement can be thought representative of a depth which
411 ~~can also be can-be-also~~ below the subskin level (typically of the order of some centimeters). Consistently with
412 figure 65, the wrfskin has a larger positive bias than modradnemo in June.

413
414 Further, as shown by figure 87, the bias between CMEMS MED DOISST and drifters is generally positive
415 anytime except in late spring/summer and autumn during nighttime. This pattern arises because of the
416 composite effect of having a temperature representative of the subskin level where and when there are data
417 from radiometers, and a temperature of about 1 m depth from the MEDFS system as first guess of the optimal
418 interpolation over cloudy regions (Pisano et al., 2022). However, the modified scheme significantly reduces the
419 difference, yielding a bias closer to the one of CMEMS MED DOISST with respect to drifters, especially during
420 April, which is the month in which the number of observations from drifters is definitely larger.

421 4.3 Comparison with EN4 objective analysis

422 Bias corrected vertical profiles gathered in an objective analysis were used to assess differences across
423 schemes along the water column. To summarize we report here only a macro subdivision into the eastern and
424 the western Mediterranean Sea, respectively in figures 98, 109. Model outputs were remapped on the same
425 vertical and horizontal grid. Looking at the mean profile averaged over all grid points in the given area, the
426 agreement is better for all simulations during summertime months, both for the eastern and the western region
427 (see figs. 98c, 109c), showing in particular that the modradnemo simulation outperforms the nemoskwrite one.
428 This is also true for the wintertime season in the eastern Mediterranean (see fig. 98b). On the other hand, in the

429 western Mediterranean all simulations tend to overestimate the signal, with our modified scheme doing a better
430 job with respect to the nemoskwrite case, with an average profile which is about 0.4°C closer to the EN4 profile.
431 However, below about 80 m depth differences across schemes vanish.

432
433 Looking in more detail at the RMSE on the top 15 m depth between each simulation and EN4 as a function of
434 the month and more detailed region subdomains shown in figure 110a, we can see how in general all simulations
435 present the same pattern for the region outside of Gibraltar Strait, which can be thought an effect related to the
436 presence of the relaxation to horizontal boundary conditions, while for all the remaining regions and months
437 the control run, the wrfskin and the modradnemo present a similar pattern, with the modradnemo reducing the
438 RMSE in most of the regions and for most of the months, especially with respect to nemoskwrite, and this is
439 particularly true over the central Mediterranean Sea, in regions like Thyrranian and Adriatic Seas.

440 4.4 Heat fluxes and vertical propagation

441 In this section we aim to characterize the differences of each scheme with respect to the control simulation.
442 We do this by specifically looking at the seasonality of Mixed Layer Depth (MLD), vertical profiles of
443 temperature in specific months and regions, and via the comparison of the net surface heat fluxes over the whole
444 Mediterranean Sea.

445
446 Compared to the Mixed Layer Depth climatology from 1969 to 2013 (Houpert et al., 2015a, Houpert et al.,
447 2015b, section 2.7), all of the tested schemes seems seem to have a similar impact on Mixed Layer Depth's
448 seasonality, with larger differences with respect climatological values being mostly located in the Eastern
449 Mediterranean Sea and during wintertime/spring (Figure 124). It may seem from this picture that there's not
450 such a huge change to prefer one method over the other considered in this paper, and this may also be because
451 of the short period simulated (2019-2021). Figure 132 show how our modified scheme allows more (less)
452 vertical propagation of the diurnal signal during summer (winter) with respect to schemes with constant e-
453 folding depth in all central regions of the Mediterranean domain (regions 2, 3, 4 as defined in figure 110a),
454 when all of them are referenced to the control simulation temperature daily minimum.

455 Indeed, from figure 132b, we can see that when all the temperature profiles for each simulation are referenced
456 to the ctrlnoskin daily minimum, there is a much wider diurnal warming signal for most of all the considered
457 depths level, with modradnemo representing an intermediate situation between the wrfskin and the nemoskwrite
458 simulation. This is probably due to the inclusion of chlorophyll-interactive variations, which allow for a better
459 representation of the variability of the mixed layer dynamics.

460 Estimates of the mean Mediterranean heat exchange between ocean and atmosphere based on previous studies
461 range from -11 to +22 W/m², with an evident dominance of negative estimates, i.e., heat loss from the ocean to
462 the atmosphere (Jordà et al., 2017, Pettenuzzo et al., 2010). Some other studies suggest that the Mediterranean
463 heat budget is close to a neutral value, -1 W/m² (Ruiz et al., 2008) or +1 W/m² (Criado et. al., 2012). Many
464 factors can contribute to such wide variability among different estimates, such as differences in the

parameterizations employed, initial and boundary conditions, and the way the physical processes, especially through the Strait of Gibraltar are modeled (Macdonalds et al., 1994, Gonzales, 2023).

As shown by table 3, all simulations on an annual basis give a negative, non-closed balance for the net surface heat flux, and modifications to include skinSST, performing very similarly one to another, bring the budget by 1.5 W/m^2 closer to zero, while ERA5 data show a positive net surface heat flux close to 5 W/m^2 . However, all estimates fall into the (large uncertain) literature-based estimates. On seasonal timescales, the inclusion of skinSST diurnal variations has the following effects:

- less net heat loss to the atmosphere during wintertime with respect to the control run (wrfskin differing from the ctrlnoskin by about 6 W/m^2 , while nemoskwrite and modradnemo having a similar impact, with a difference of about 4 W/m^2 with respect to the control run);
- in springtime, all simulations show a positive imbalance, with the highest difference with respect to the control run of about 1 W/m^2 in the modradnemo simulation;
- during summer, our modified scheme brings on average about 3 W/m^2 more than the control simulation into the basin, yielding an estimate which is closer to ERA5;
- in autumn, our scheme cools down more than the control (about 2 W/m^2), being the farthest simulation from ERA5 estimate, while traditional schemes tend to have a less negative net heat input.

All seasons except spring show larger difference with respect to ERA5 fluxes, with underestimation in summer, and overestimation during winter and autumn, resulting in a bias of about 10 W/m^2 with respect to the net heat flux annual budget in ERA5.

5 Summary and Conclusions

In this paper we studied the sensitivity of a regional coupled ocean-atmosphere-hydrological discharge regional model on the Mediterranean Sea to prognostic schemes for skin sea surface temperature. Specifically, we developed a new scheme which allows for spatial and temporal variations of the warm layer's extent according to seawater's transparency conditions. This is possible by using tabulated solar extinction coefficients already used in the ocean model, and inverting the functional form which determines how the solar radiation varies along the vertical direction to find the depth at which this latter drops ~~by-to~~ $1/e$ from its surface value.

We simulated the period 2019-2021, analyzing hourly model outputs, and comparing aggregated results with satellite, objectively analyzed and drifters data. Overall, the comparison with data shows that the new scheme improves what is already implemented in NEMO, e.g. mean diurnal warming amplitudes are closer to satellite observations in winter, spring and autumn, not being much worse than other existing schemes in summer, at least looking at maps of mean diurnal warming amplitude grouped by seasons. Looking to the typical

499 temperature profile in both the eastern and the western Mediterranean Sea, non-negligible differences across
500 schemes stay confined in the topmost 20m (100m) of depth during summertime (wintertime). Regionally,
501 typical profiles are warmer than EN4 observation year-round for western regions (regions -1,1,2) especially in
502 winter, while regions in the east show a smaller RMSE in the topmost meters for basically all the regions and
503 months when comparing modradnemo to nemoskwrite. The Adriatic Sea has a systematically higher RMSE
504 with respect to EN4 in all the tested methods, for the whole period considered. In the central regions, the new
505 scheme penetrates temperature anomalies more (less) during summer (winter) months, having a less intense
506 mean diurnal warming amplitude signal in summer, especially over the upper few meters (the converse holds
507 for wintertime values). Therefore, with respect to the ctrlnoskin simulation, nemoskwrite shows the coldest
508 signal, the wrskin the hottest, and our modification modradnemo constitutes the middle situation, with milder
509 summer and winter than the control run. Our interpretation is that within modradnemo, the chl-interactive e-
510 folding depths allow, where and when necessary, the warm layer to become a little deeper than in the already
511 existing scheme (nemoskwrite), depending on chl-variations. For these space-time points, solar penetration is
512 increased and so it tends to make warmer the warm layer. Therefore, future research efforts should be devoted
513 to the better characterization of this aspect, especially to understand if the modified vertical penetration of heat
514 has some particular effect on the dynamics of the mixed layer (see Song and Yu, 2017 and references therein).
515 Furthermore, testing the implementation within NEMO of more sophisticated radiative transfer models (such
516 as the one of Ohlmann and Siegel 2000), or the development of deep learning based parameterizations are
517 underway as future research efforts. On a long-term perspective, the method needs to be tested also in other
518 areas and for longer periods, which can increase the results' certainty and allow for usage in investigating
519 impacts on relevant climate large-scale phenomena, where the role of an improved diurnal warming signal
520 could be more relevant (Bernie et al., 2007, Bernie et al., 2008). These includes phenomena and physical
521 processes such as propagation of Marine Heat Waves (MHW) or deep water formation and deep convective
522 events.

525 *Code and data availability*

526 The NEMO ocean model code (v4.0.7) is available at <https://forge.ipsl.jussieu.fr/nemo/wiki>.

528 The WRF atmospheric model code (v4.3.3) is available at <https://github.com/wrf-model/WRF>.

529 The HD hydrological discharge model (v5.1) is available at <https://zenodo.org/record/5707587#.Y-0VQ3bMKUk>.

530 The frozen version of the MESMARv1 code used in this manuscript is available at:
531 <https://doi.org/10.5281/zenodo.7898938>.

532 CMEMS MED DOISST Data downloaded from [CMEMS portal](#).

533 Chlorophyll data are freely available from [CMEMS portal](#).

534 The iQuam data version of this study used is V2.1, downloaded from the National Environmental Satellite,
535 Data, and Information Service Satellite Applications and Research [NOAA NESDIS STAR portal](#).

536 Gridded analyses of EN4 profiles are distributed from the [MetOffice Hadley Centre Observations](#) (we used
537 version 4.2.1).

538 ERA5 data are freely available after registration on the [Climate Data Store \(CDS\) by Copernicus Climate
539 Change Service \(C3S\)](#).

540 MLD data are distributed on a 0.25 degree regular grid, and freely available from the [Sea Open Scientific Data
541 Publication SEANOE portal](#).

542 Minimal data and scripts used within the manuscript to reproduce the figures in the manuscript are available at
543 this link:

544 <https://zenodo.org/records/10451206>

558 *Acknowledgments.* We specifically acknowledge Olivier Marti (LSCE/IPSL) and Aurore Voldoire (CNRM-
559 CNRS) for fruitful discussion during the 6th Workshop on Coupling Technologies for ESM held from 18 to 20
560 January 2023 in Toulouse, and Sophie Valcke (CERFACS) for their valuable support in the use of the NEMO
561 and WRF interfaces to the OASIS coupler. This Research is supported by ICSC – National Research Center for
562 High Performance Computing, Big Data and Quantum Computing, funded by Ministero dell'Istruzione,
563 dell'Università e della Ricerca through the NextGenerationEU programme.

564

565 *Author Contributions.* VdT and AS conceived the study and designed the experiments to conduct, VdT
566 Performed the simulation and data analysis, data downloading and writing of the first draft, VdT, DC, YH, CY,
567 VA, AP, DC, RS and AS equally contributed to discuss and interpret the results, finalizing the draft.

568

569 *Competing Interests.* All authors declare they have no competing interests.

Figures

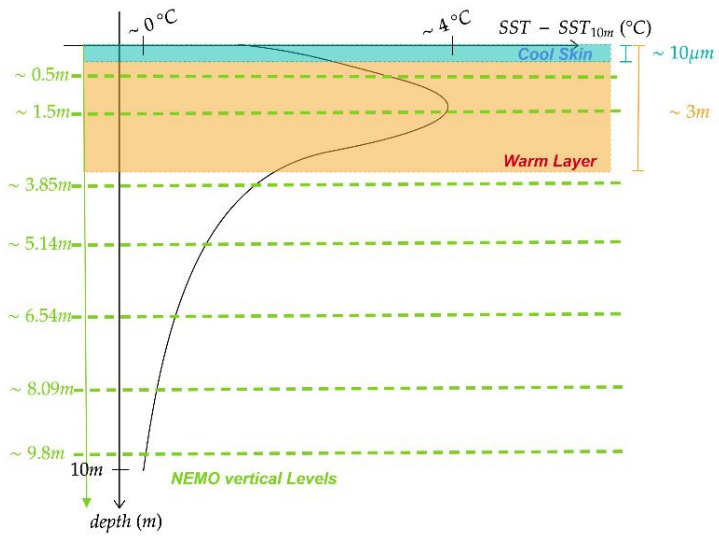
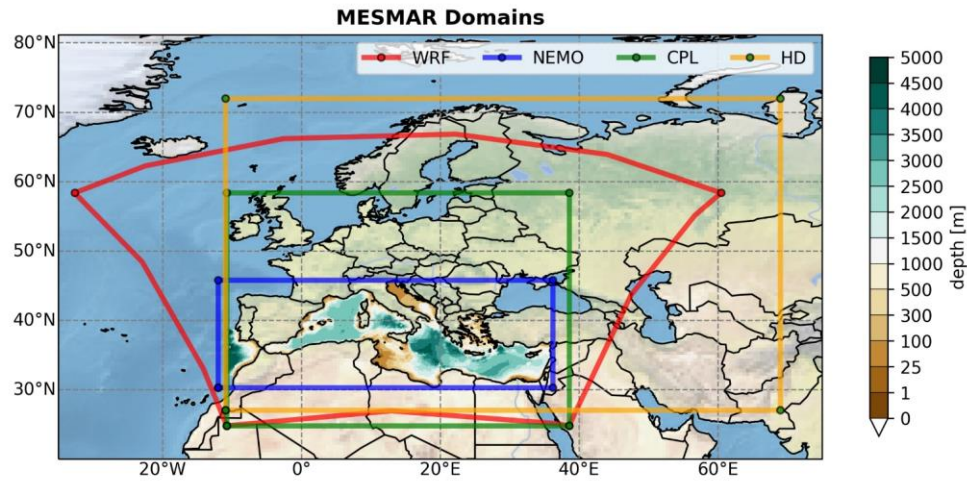


Figure 1. Sketch of the cool skin and warm layer adapted from Donlon et al., 2007. Vertical discretization of NEMO levels is shown in green (not perfectly in scale with the underlying y-axis).

576
577



ha formattato: Tipo di carattere: (Predefinito) Cambria, 11 pt

Formattato: Normale, Rientro: Sinistro: 0 cm, SpazioDopo: 0 pt

578

579 **Figure 12:** The modeling system domain: WRF, NEMO, HD and boundaries for the coupling mask are
580 respectively in red, blue, orange, and green. Contour filled plot shows the ocean model bathymetry.

581

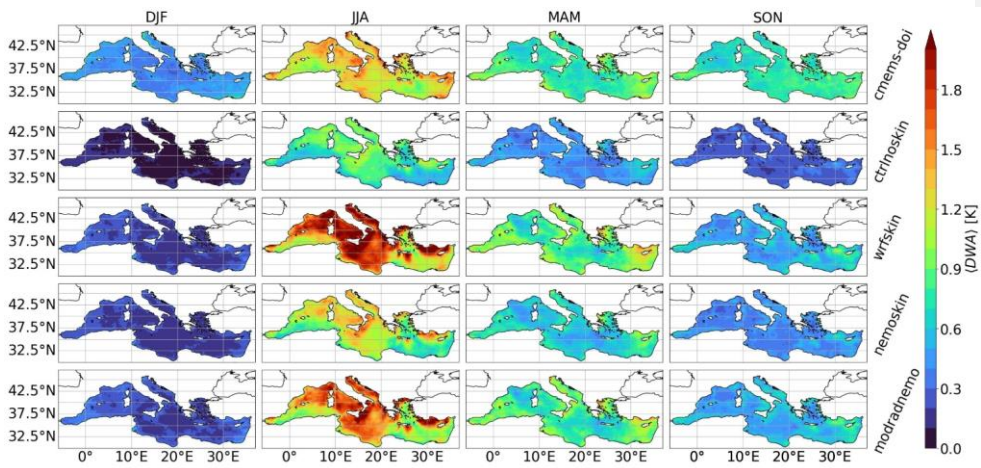
582

583

584 **Figure 32:** Panel 2a shows two different formulations frequently used for the transmission coefficient
 585 expression: the red curve shows the formulation of Soloviev, 1982, while the green curve the one defined in
 586 Soloviev and Schluskel, 1996. Panel 2b shows e-folding depth estimates from Mediterranean Chlorophyll
 587 climatology of Volpe et al., 2019: lowest values touch the 2.5 meters.

21

588
589



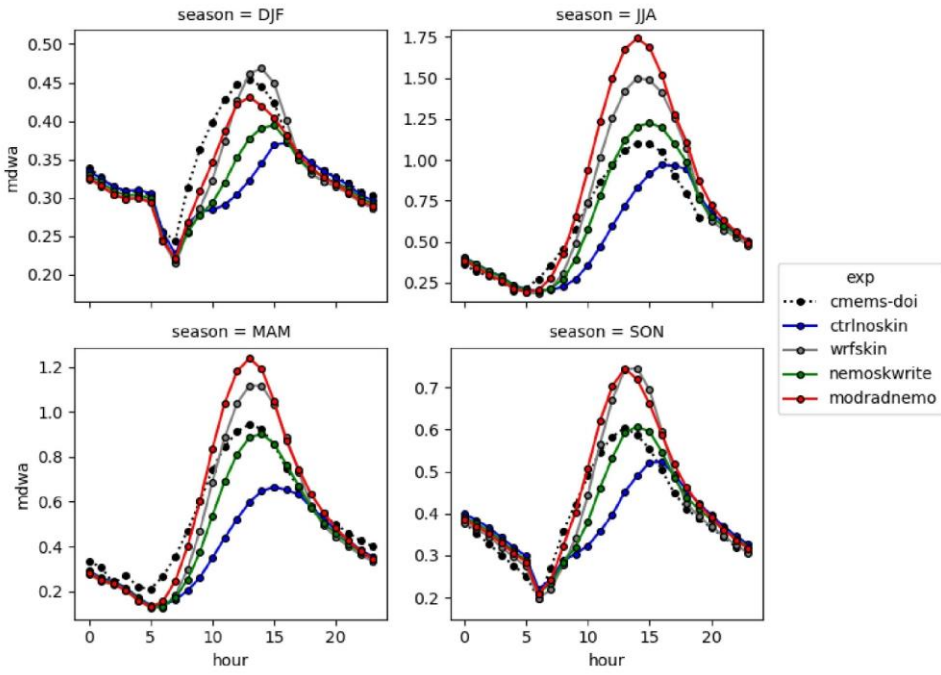
590

591 **Figure 34:** Mean diurnal warming amplitude averaged over seasons (on columns), for each case (row): the first
592 row is the CMEMS MED DOISST data, followed in order by the control simulation, wrf5skin, nemoskwrite and
593 modradnemmo.

594

595

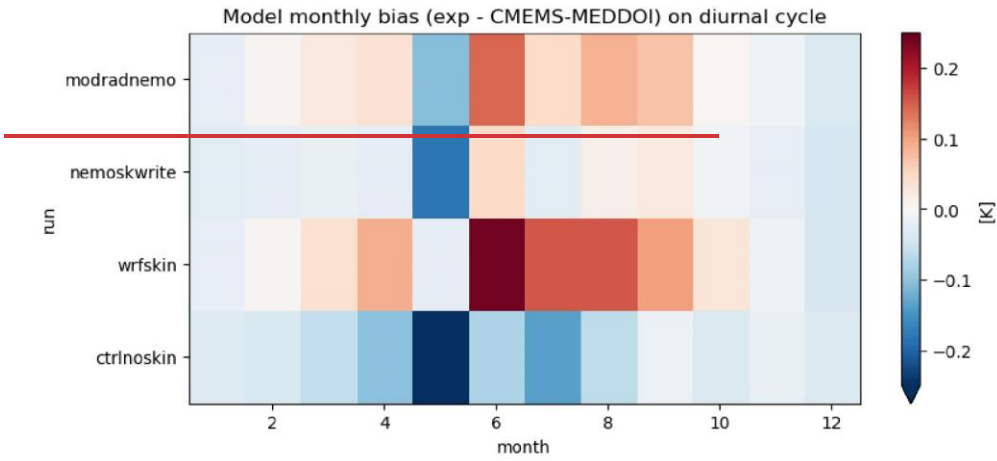
596



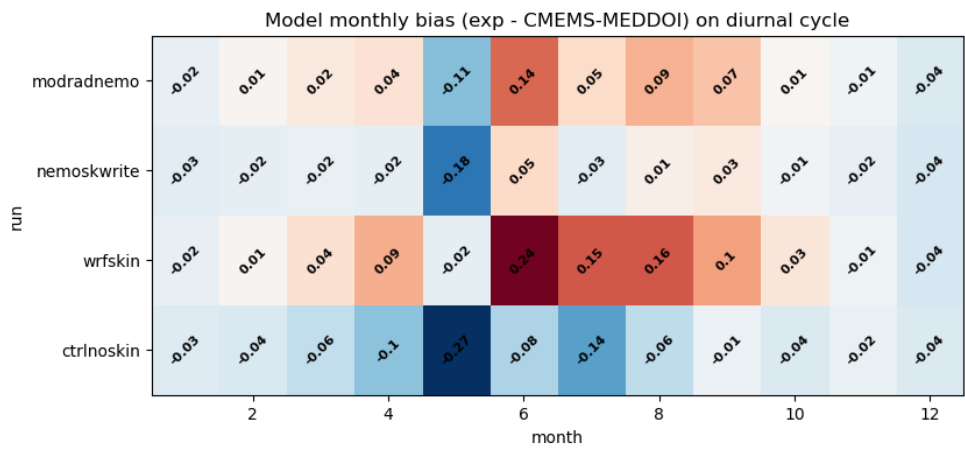
597

598 **Figure 54:** Seasonality of the diurnal cycle averaged over the whole Mediterranean Sea, masking out regions
599 in time and space where the percentage of model data in CMEMSDOI is greater than 50%.
600

601



602



603

604 **Figure 65:** Monthly averaged values for the time series of spatial mean diurnal cycle over the Mediterranean
 605 Sea (bias with respect to CEMS MED DOISSST)

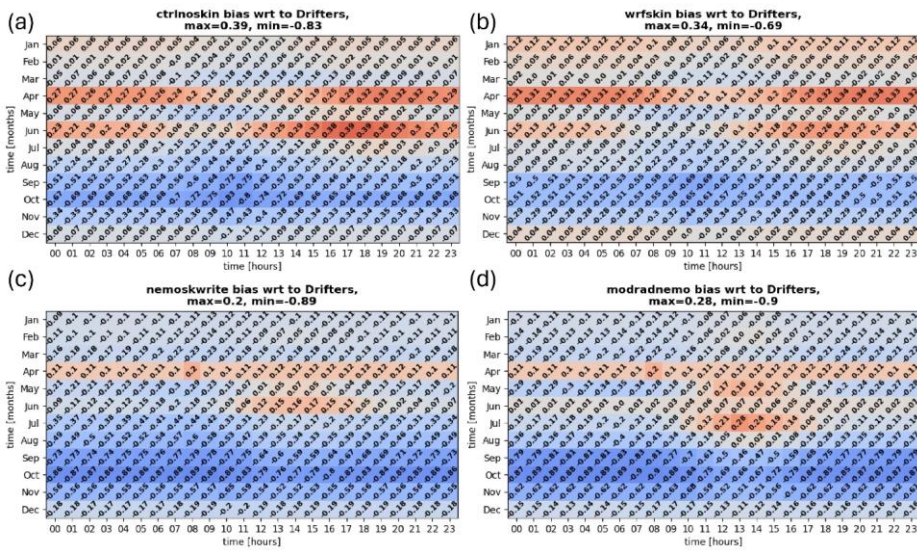
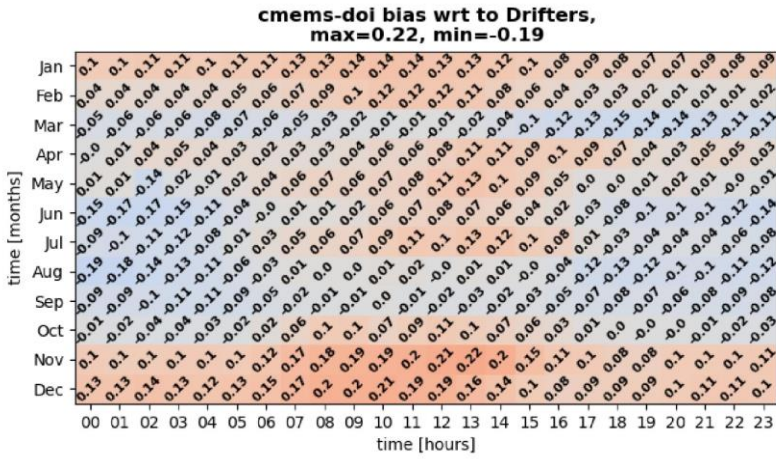


Figure 76: Bias with respect to measurements averaged over drifters' locations as a function of the month and the time of the day. Panels 6a, 6b, 6c, 6d show respectively the results for all the simulations carried out in the present study. Confidence on these numbers can be supported by the numbers of measurements reported in table S1.

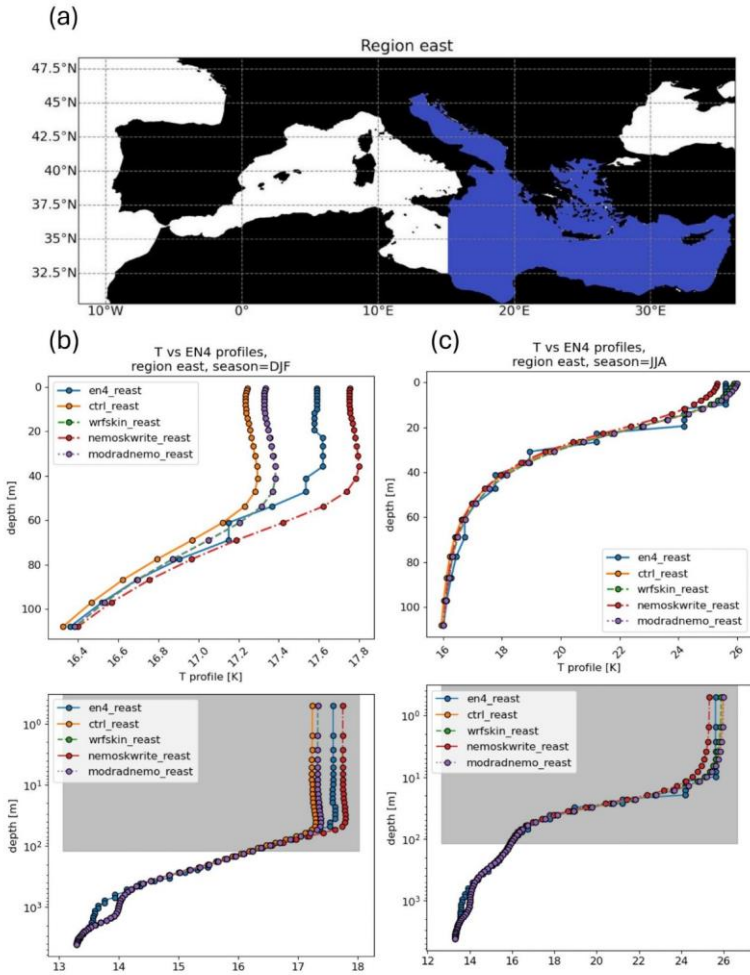
607
 608
 609
 610
 611
 612
 613

614



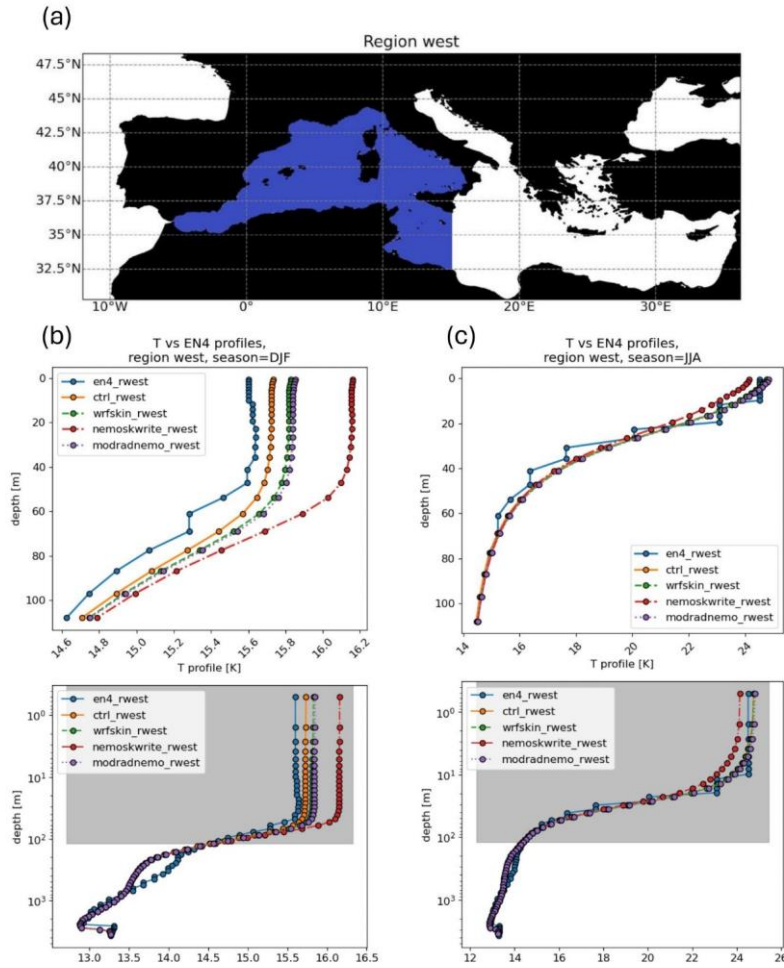
615

616 **Figure 87:** Bias with respect to measurements averaged over drifters' locations as a function of the month and
617 time of the day, for CMEMS MED DOISST data.
618



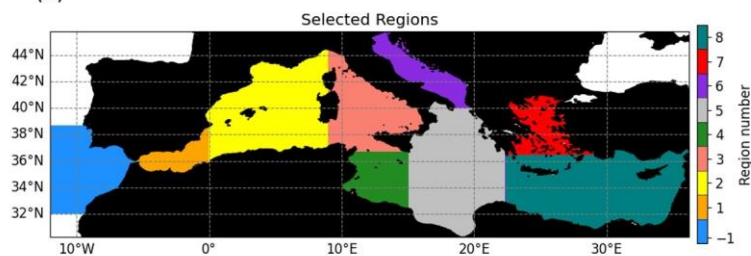
620
621
622
623
624

Figure 98: Spatial average of profiles within the eastern Mediterranean Sea, during winter and summer. Panel 98a shows the eastern region, while 98b, 98c show respectively wintertime and summertime spatially averaged profiles within the top 100 m in the upper part, on the bottom the whole depth range on a logarithmic scale.

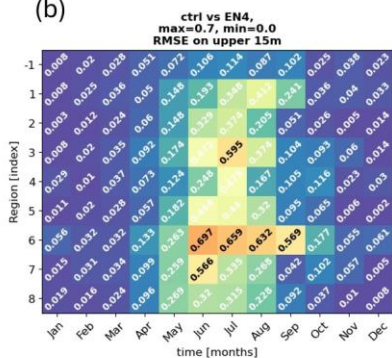


626
627 **Figure 109:** Spatial average of profiles within the eastern Mediterranean Sea, during winter and summer. Panel
628 109a shows the eastern region, while 109b, 109c show respectively wintertime and summertime spatially-
629 averaged profiles within the top 100 m in the upper part, on the bottom the whole depth range on a logarithmic
630 scale.
631

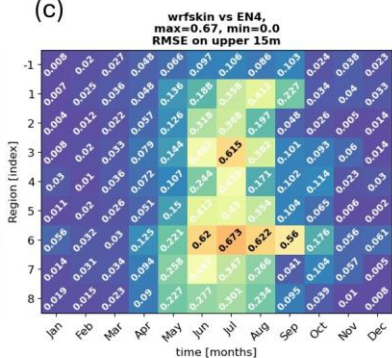
(a)



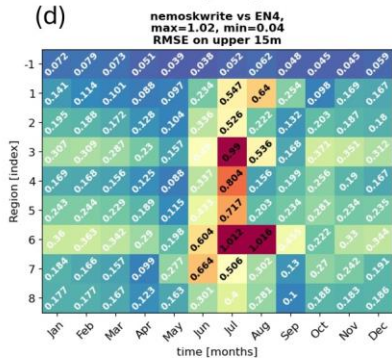
(b)



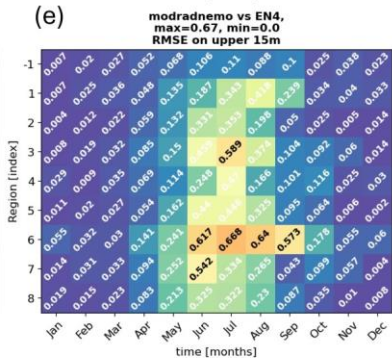
(c)

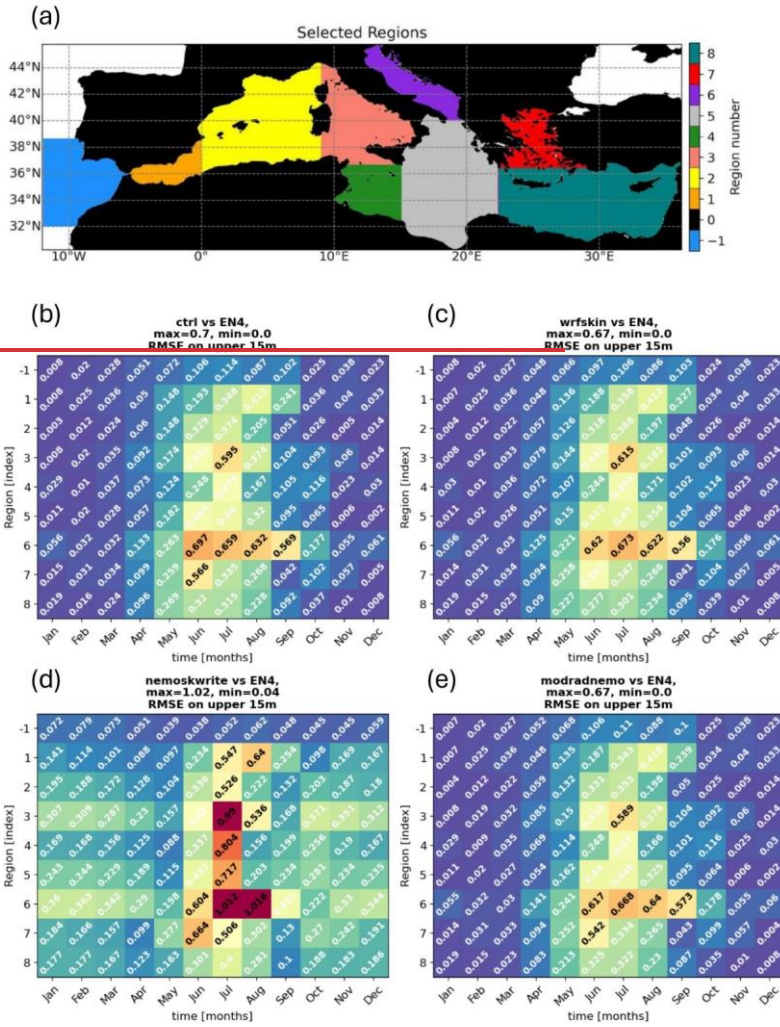


(d)

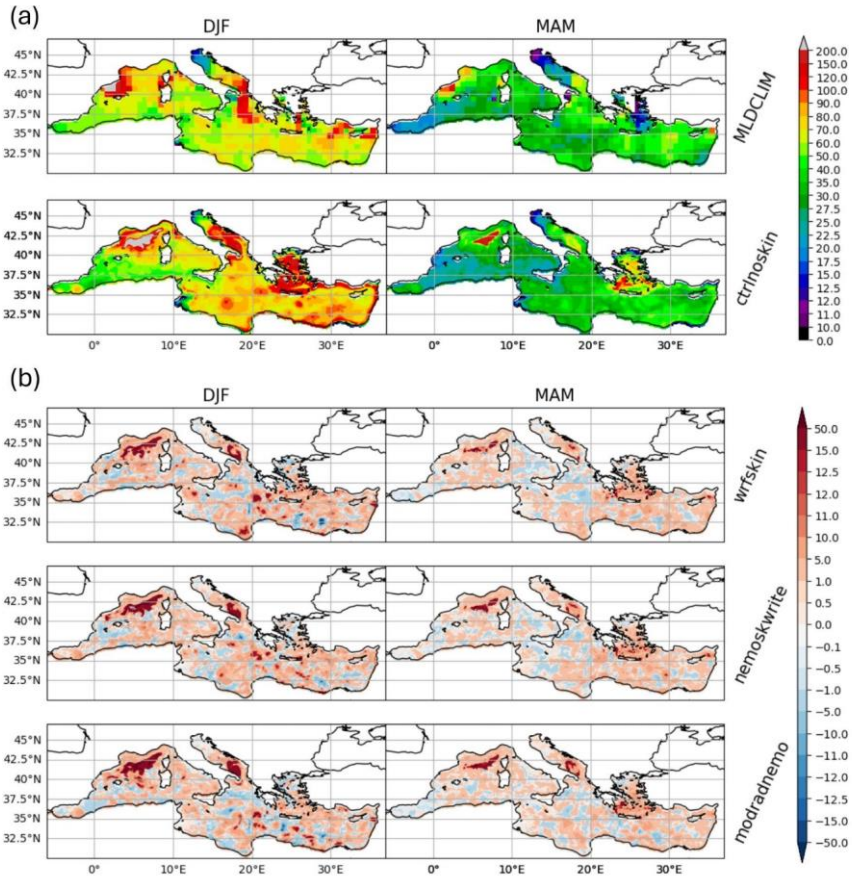


(e)

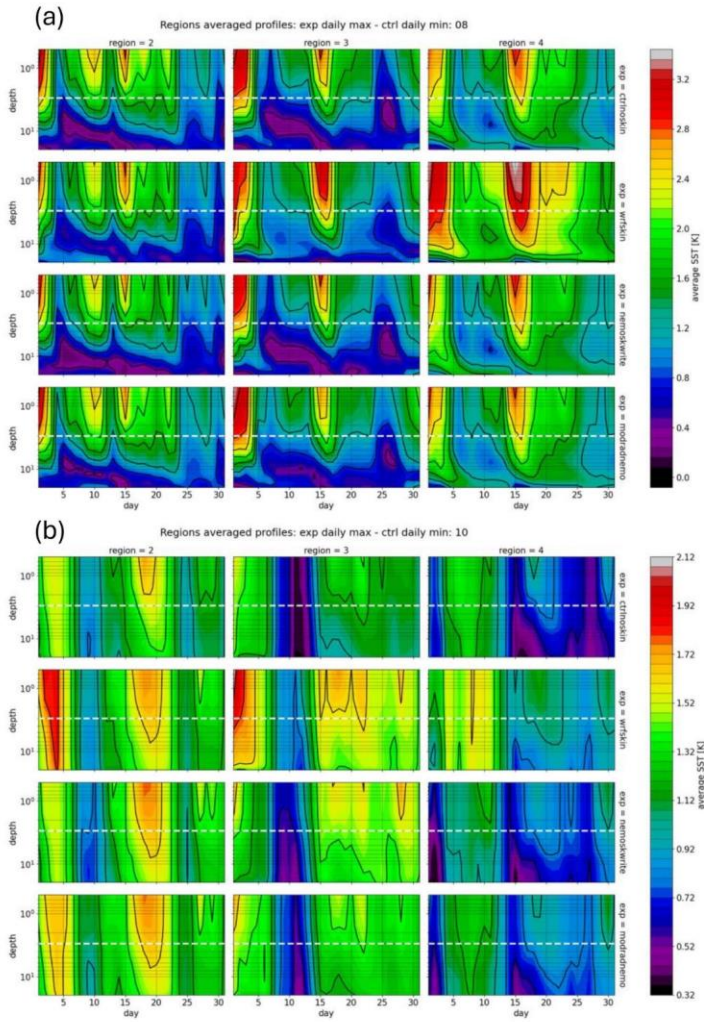




633
 634 **Figure 110:** RMSE on the top 15m of the difference between regionally averaged profiles between each
 635 simulation and EN4, displayed as a function of the region and the particular month. Division in regions is
 636 reported in panel 110a, while 110b, 110c, 110d, 10e show respectively the results for all the simulations carried
 637 out in the present study.
 638



639
 640 **Figure 12:** Maps of DJF, MAM of mixed layer depth for the climatology and for the control simulation in
 641 panel (a). Panel (b) shows the difference of the control with respect to each simulation. Units are meters.
 642
 643
 644
 645
 646
 647
 648
 649
 650
 651
 652
 653
 654
 655
 656
 657
 658



660
 661
 662
 663
 664
 665
 666

Figure 132: Hovmöller plots for spatial average of model outputs temperature profiles in the regions 2,3,4 as defined by figure 119a. Each row shows the difference between daily maxima for the given experiment minus the daily minima for the control simulation. The white dashed line traces the $z = 3m$ line of the depth used as reference for the base of the warm layer as in ZB05 scheme Zeng and Beljaars, 2005. Panel 132a shows August, panel 132b shows October.

667
668
669

Tables

Simulation	Scheme active	Extinction coefficients in Warm Layer
ctrlnoskin	None	None
wrfskin	ZB05	SS82
nemoskwrite	ZB05+A02+T10	G09
modradnemo	ZB05+A02+T10	R-G-B + chl e-folding

670 **Table 1:** Overview of the simulations performed

671

Wavelength [μm]	i	a_i	b_i [m^{-1}]
0.3-0.6	1	0.2370	1.488×10^{-1}
0.6-0.9	2	0.3600	4.405×10^{-1}
0.9-1.2	3	0.1790	3.175×10^1
1.2-1.5	4	0.0870	1.825×10^2
1.5-1.8	5	0.0800	1.201×10^3
1.8-2.1	6	0.0246	7.937×10^3
2.1-2.4	7	0.0250	3.195×10^3
2.4-2.7	8	0.0070	1.279×10^4
2.7-3.0	9	0.0004	6.944×10^4

672 **Table 2:** Parameters for the Transmission coefficient following Soloviev and Schlu'ssel, 1996, in which the
673 first coefficients is the average between the one corresponding to I, IA, IB, II, and III Jerlov optical water types.
674 This is currently implemented in NEMO.

simulation	DJF	MAM	JJA	SON	Annual
ctrlnoskin	-173.31	133.92	75.56	-66.40	-7.55
wrfskin	-168.83	134.19	76.51	-65.87	-5.97
nemoskwrite	-169.28	133.79	76.77	-65.72	-6.10
modradnemo	-169.06	134.87	78.16	-68.13	-6.04
ERA5	-140.36	133.24	81.96	-53.46	5.35

Table 3: Averaged surface net heat flux over the Mediterranean Sea (W/m^2): seasonal and annual spatial averaged mean values.

675
676
677

678

679

680 **References**

681

682 Artale, V., Iudicone, D., Santoleri, R., Rupolo, V., Marullo, S., and d'Ortenzio, F.: Role of surface fluxes in
683 ocean general circulation models using satellite Sea Surface Temperature: Validation of and sensitivity to the
684 forcing frequency of the Mediterranean thermohaline circulation. *Journal of Geophysical Research: Oceans*,
685 107(C8):29–1, 2002.

686 Bernie, D., Guilyardi, E., Madec, G., Slingo, J., and Woolnough, S.: Impact of resolving the diurnal cycle in an
687 ocean–atmosphere GCM. Part 1: A diurnally forced OGCM. *Climate Dynamics*, 29:575–590, 2007.

688 Bernie, D., Guilyardi, E., Madec, G., Slingo, J. M., Woolnough, S. J., and Cole, J.: Impact of resolving the
689 diurnal cycle in an ocean–atmosphere GCM. Part 2: A diurnally coupled C-GCM. *Climate dynamics*, 31:909–
690 925, 2008.

691 Chen, S. S. and Houze Jr, R. A.: Diurnal variation and life-cycle of deep convective systems over the tropical
692 pacific warm pool. *Quarterly Journal of the Royal Meteorological Society*, 123(538):357–388, 1997.

693 Craig, A., Valcke, S., and Coquart, L.: Development and performance of a new version of the OASIS coupler,
694 OASIS3-MCT 3.0. *Geoscientific Model Development*, 10(9):3297– 3308, 2017.

695 Criado-Aldeanueva, F., Soto-Navarro, F. J., & García-Lafuente, J.: Seasonal and interannual variability of
696 surface heat and freshwater fluxes in the Mediterranean Sea: Budgets and exchange through the Strait of
697 Gibraltar. *International Journal of Climatology*, 32(2), 286–302, 2012.

698 [Vincenzo de Toma. \(2024\). Skin Sea Surface Temperature schemes in coupled ocean-atmosphere modeling:
699 the impact of chlorophyll-interactive e-folding depth. Intermediate results and scripts to produce the figures.
700 Zenodo. <https://doi.org/10.5281/zenodo.10818183>](https://doi.org/10.5281/zenodo.10818183)

701 Donlon, C., Robinson, I., Casey, K., Vazquez-Cuervo, J., Armstrong, E., Arino, O., Gentemann, C., May, D.,
702 LeBorgne, P., Pioll'e, J., et al.: The global ocean data assimilation experiment high-resolution Sea Surface
703 Temperature pilot project. *Bulletin of the American Meteorological Society*, 88(8):1197–1214, 2007.

704 Fairall, C., Bradley, E. F., Godfrey, J., Wick, G., Edson, J. B., and Young, G.: Cool-skin and warm-layer effects
705 on Sea Surface Temperature. *Journal of Geophysical Research: Oceans*, 101(C1):1295–1308, 1996.

706 Gentemann, C. L., Minnett, P. J., and Ward, B.: Profiles of ocean surface heating (POSH): A new model of
707 upper ocean diurnal warming. *Journal of Geophysical Research: Oceans*, 114(C7), 2009.

708 Gonzalez, N. M.: Multi-scale modelling of Gibraltar Straits and its regulating role of the Mediterranean climate
709 (*Doctoral dissertation, Université Paul Sabatier-Toulouse III*), 2023.

710 Gouretski, V. and Cheng, L.: Correction for systematic errors in the global dataset of temperature profiles from
711 mechanical bathythermographs. *Journal of Atmospheric and Oceanic Technology*, 37(5):841–855, 2020.

712 Gouretski, V. and Reseghetti, F.: On depth and temperature biases in bathythermograph data: Development of
713 a new correction scheme based on analysis of a global ocean database. *Deep Sea Research Part I:
714 Oceanographic Research Papers*, 57(6):812– 833, 2010.

715 Hagemann, S., Stacke, T., & Ho-Hagemann, H. T.: High resolution discharge simulations over Europe and the
716 Baltic Sea catchment. *Frontiers in Earth Science*, 8, 12, 2020.

717 Hersbach, H., Bell, B., Berrisford, P., Hirahara, S., Hor'anyi, A., Mun'oz-Sabater, J., Nicolas, J., Peubey, C.,
718 Radu, R., Schepers, D., et al.: The ERA5 global reanalysis. *Quarterly Journal of the Royal Meteorological
719 Society*, 146(730):1999–2049, 2020.

- 720 Houpert L, Testor P, Durrieu de Madron X.: Gridded climatology of the Mixed Layer (Depth and Temperature),
 721 the bottom of the Seasonal Thermocline (Depth and Temperature), and the upper-ocean Heat Storage Rate
 722 for the Mediterrean Sea. SEANOE. <https://doi.org/10.17882/46532.2015a>.
- 723 Houpert, L., Testor, P., De Madron, X. D., Somot, S., D'ortenzio, F., Estournel, C., & Lavigne, H.: Seasonal
 724 cycle of the mixed layer, the seasonal thermocline and the upper-ocean heat storage rate in the Mediterranean
 725 Sea derived from observations. *Progress in Oceanography*, 132, 333-352, 2015b.
- 726 Jansen, E., Pimentel, S., Tse, W. H., Denaxa, D., Korres, G., Mirouze, I., & Storto, A.: Using canonical
 727 correlation analysis to produce dynamically based and highly efficient statistical observation operators.
 728 *Ocean Science*, 15(4), 1023-1032, 2019.
- 729 Jerlov, N. G.: *Optical Oceanography*. Amsterdam, London and New York: Elsevier Publishing Co, 1968.
- 730 Jordà, G., Von Schuckmann, K., Josey, S. A., Caniaux, G., García-Lafuente, J., Sammartino, S., ... & Macías,
 731 D.: The Mediterranean Sea heat and mass budgets: Estimates, uncertainties and perspectives. *Progress in*
 732 *Oceanography*, 156, 174-208, 2017.
- 733 Karagali, I. and Høyer, J.: Observations and modeling of the diurnal SST cycle in the North and Baltic seas.
 734 *Journal of Geophysical Research: Oceans*, 118(9):4488–4503, 2013.
- 735 Kawai, Y. and Wada, A.: Diurnal Sea Surface Temperature variation and its impact on the atmosphere and
 736 ocean: A review. *Journal of oceanography*, 63:721–744, 2007.
- 737
- 738 Large, W. G., McWilliams, J. C., and Doney, S. C.: Oceanic vertical mixing: A review and a model with a
 739 nonlocal boundary layer parameterization. *Reviews of geophysics*, 32(4):363–403, 1994.
- 740 Lee, Z., Du, K., Arnone, R., Liew, S., & Penta, B. (2005). Penetration of solar radiation in the upper ocean: A
 741 numerical model for oceanic and coastal waters. *Journal of Geophysical Research: Oceans*, 110(C9).
- 742 Lengaigne, M., Menkes, C., Aumont, O., Gorgues, T., Bopp, L., André, J. M., & Madec, G.: Influence of the
 743 oceanic biology on the tropical Pacific climate in a coupled general circulation model. *Climate Dynamics*,
 744 28, 503-516, 2007.
- 745 Leonelli, F. E., Bellacicco, M., Pitarch, J., Organelli, E., Buongiorno Nardelli, B., De Toma, V., ... & Santoleri,
 746 R. (2022). Ultra-oligotrophic waters expansion in the North Atlantic Subtropical Gyre revealed by 21 years
 747 of satellite observations. *Geophysical Research Letters*, 49(21), e2021GL096965.
- 748 Macdonald, A. M., Candela, J., & Bryden, H. L.: An estimate of the net heat transport through the Strait of
 749 Gibraltar. *Seasonal and Interannual Variability of the Western Mediterranean Sea*, 46, 13-32, 1994.
- 750 Marullo, S., Pitarch, J., Bellacicco, M., Sarra, A. G. d., Meloni, D., Monteleone, F., Sferlazzo, D., Artale, V.,
 751 and Santoleri, R.: Air–sea interaction in the central Mediterranean Sea: Assessment of reanalysis and satellite
 752 observations. *Remote Sensing*, 13(11):2188, 2021.
- 753 Marullo, S., Santoleri, R., Banzon, V., Evans, R. H., & Guarracino, M.: A diurnal-cycle resolving sea surface
 754 temperature product for the tropical Atlantic. *Journal of Geophysical Research: Oceans*, 115(C5), 2010.
- 755 Marullo, S., Minnett, P. J., Santoleri, R., & Tonani, M.: The diurnal cycle of sea-surface temperature and
 756 estimation of the heat budget of the Mediterranean S ea. *Journal of Geophysical Research: Oceans*, 121(11),
 757 8351-8367, 2016.
- 758 Minnett, P., Alvera-Azc´arate, A., Chin, T., Corlett, G., Gentemann, C., Karagali, I., Li, X., Marsouin, A.,
 759 Marullo, S., Maturi, E., et al.: Half a century of satellite remote sensing of Sea Surface Temperature. *Remote*
 760 *Sensing of Environment*, 233:111366, 2019.
- 761 Morel, A., & Antoine, D. (1994). Heating rate within the upper ocean in relation to its bio–optical state. *Journal*
 762 of Physical Oceanography, 24(7), 1652-1665.

ha formattato: Tipo di carattere: Corsivo

ha formattato: Italiano (Italia)

ha formattato: Tipo di carattere: Corsivo

ha formattato: Tipo di carattere: Corsivo

763 Morel, A., & Berthon, J. F.: Surface pigments, algal biomass profiles, and potential production of the euphotic
764 layer: Relationships reinvestigated in view of remote-sensing applications. *Limnology and oceanography*,
765 34(8), 1545-1562, 1989.

766 NEMO System Team: *NEMO ocean engine*, 1288-1619 (isnn) edition, 2019.

767 [Ohlmann, J. C., Siegel, D. A., & Mobley, C. D. \(2000\). Ocean radiant heating. Part I: Optical influences. *Journal*
768 *of Physical Oceanography*, 30\(8\), 1833-1848.](#)

769 [Ohlmann, J. C., & Siegel, D. A. \(2000\). Ocean radiant heating. Part II: Parameterizing solar radiation
770 transmission through the upper ocean. *Journal of Physical Oceanography*, 30\(8\), 1849-1865.](#)

771 Penny, S. G., Akella, S., Balmaseda, M. A., Browne, P., Carton, J. A., Chevallier, M., Counillon, F., Domingues,
772 C., Frolov, S., Heimbach, P., et al.: Observational needs for improving ocean and coupled reanalysis, S2S
773 prediction, and decadal prediction. *Frontiers in Marine Science*, 6:391, 2019.

774 Pettenuzzo, D., Large, W. G., & Pinardi, N.: On the corrections of ERA-40 surface flux products consistent
775 with the Mediterranean heat and water budgets and the connection between basin surface total heat flux and
776 NAO. *Journal of Geophysical Research: Oceans*, 115(C6), 2010.

777 Pisano, A., Ciani, D., Marullo, S., Santoleri, R., and Buongiorno Nardelli, B.: A new operational mediterranean
778 diurnal optimally interpolated SST product within the copernicus marine environment 2 monitoring service
779 3. *Earth System Science Data Discussions*, 2022:1–26, 2022.

780 Ruiz, S., Gomis, D., Sotillo, M. G., & Josey, S. A.: Characterization of surface heat fluxes in the Mediterranean
781 Sea from a 44-year high-resolution atmospheric data set. *Global and Planetary Change*, 63(2-3), 258-274,
782 2008.

783 Saunders, P. M.: The temperature at the ocean-air interface. *Journal of Atmospheric Sciences*, 24(3):269–273,
784 1967.

785 Skamarock, W. C., Klemp, J. B., Dudhia, J., Gill, D. O., Liu, Z., Berner, J., Wang, W., Powers, J. G., Duda, M.
786 G., Barker, D. M., et al.: A description of the advanced research WRF model version 4. *National Center for*
787 *Atmospheric Research: Boulder, CO, USA*, 145(145):550, 2019.

788 Soloviev, A.: On the vertical structure of the ocean thin surface layer at light wind. *Dokl. Acad. Sci. USSR*,
789 *Earth Sci. Serr.*, pages 751–760, 1982.

790 Soloviev, A. and Lukas, R.: Observation of large diurnal warming events in the near-surface layer of the western
791 equatorial pacific warm pool. *Deep Sea Research Part I: Oceanographic Research Papers*, 44(6):1055–1076,
792 1997.

793 Soloviev, A. and Lukas, R.: The near-surface layer of the ocean: structure, dynamics and applications, *volume*
794 *48. Springer Science & Business Media*, 2013.

795 Soloviev, A. V. and Schlüssel, P.: Evolution of cool skin and direct air-sea gas transfer coefficient during
796 daytime. *Boundary-Layer Meteorology*, 77(1):45–68, 1996.

797 Song, X. and Yu, L.: Air-sea heat flux climatologies in the Mediterranean Sea: Surface energy balance and its
798 consistency with ocean heat storage. *Journal of Geophysical Research: Oceans*, 122(5):4068–4087, 2017.

799 Storto, A., Alvera-Azcárate, A., Balmaseda, M. A., Barth, A., Chevallier, M., Counillon, F., ... & Zuo, H.: Ocean
800 reanalyses: recent advances and unsolved challenges. *Frontiers in Marine Science*, 6, 418, 2019.

801 Storto, A. and Oddo, P.: Optimal assimilation of daytime SST retrievals from SEVIRI in a regional ocean
802 prediction system. *Remote Sensing*, 11(23):2776, 2019.

803

ha formattato: Tipo di carattere: Corsivo

ha formattato: Tipo di carattere: Corsivo

804 Storto, A., Hesham Essa, Y., de Toma, V., Anav, A., Sannino, G., Santoleri, R., & Yang, C.: MESMAR v1: A
805 new regional coupled climate model for downscaling, predictability, and data assimilation studies in the
806 Mediterranean region. *Geoscientific Model Development Discussions*, 2023, 1-40, 2023.
807
808 Takaya, Y., Bidlot, J.-R., Beljaars, A. C., and Janssen, P. A.: Refinements to a prognostic scheme of skin Sea
809 Surface Temperature. *Journal of Geophysical Research: Oceans*, 115(C6), 2010.
810
811 Tu, C.-Y. and Tsuang, B.-J.: Cool-skin simulation by a one-column ocean model. *Geophysical research letters*,
32(22), 2005.
812
813 Valdivieso, M., Haines, K., Balmaseda, M., Chang, Y. S., Drevillon, M., Ferry, N., ... & Andrew Peterson, K.:
814 An assessment of air–sea heat fluxes from ocean and coupled reanalyses. *Climate Dynamics*, 49, 983-1008,
2017.
815
816 Volpe, G., Colella, S., Brando, V. E., Forneris, V., La Padula, F., Di Cicco, A., Sammartino, M., Bracaglia, M.,
817 Artuso, F., and Santoleri, R.: Mediterranean ocean colour level 3 operational / multi-sensor processing. *Ocean
Science*, 15(1):127–146, 2019.
818
819 Ward, B.: Near-surface ocean temperature. *Journal of Geophysical Research: Oceans*, 111(C2), 2006.
820
821 While, J., Mao, C., Martin, M., Roberts-Jones, J., Sykes, P., Good, S., and McLaren, A.: An operational analysis
822 system for the global diurnal cycle of Sea Surface Temperature: implementation and validation. *Quarterly
823 Journal of the Royal Meteorological Society*, 143(705):1787–1803, 2017.
824
825 Xu, F. and Ignatov, A.: In situ SST quality monitor (i-quam). *Journal of Atmospheric and Oceanic Technology*,
31(1):164–180, 2014.
826
827 Zeng, X. and Beljaars, A.: A prognostic scheme of sea surface skin temperature for modeling and data
828 assimilation. *Geophysical Research Letters*, 32(14), 2005.
829
830 Zhang, R., Zhou, F., Wang, X., Wang, D., & Gulev, S. K.: Cool skin effect and its impact on the computation
831 of the latent heat flux in the South China Sea. *Journal of Geophysical Research: Oceans*, 126(1),
832 2020JC016498, 2021.
833
834 Zuo, H., Balmaseda, M. A., Mogensen, K., & Tietsche, S.: OCEAN5: the ECMWF ocean reanalysis
system and its real-time analysis component (p. 44). Reading, UK: European Centre for Medium-
Range Weather Forecasts, 2018.